Article

Lattice Compensation to Jahn−Teller Distortion in Na-Rich Manganese Hexacyanoferrate for Li-Ion Storage: An Operando Study

Angelo Mullaliu, Mattia Gaboardi, Jasper Rikkert Plaisier, Stefano Passerini,* and Marco Giorgetti*

Cite This: *ACS Appl. Energy Mater.* 2020, 3, 5728−5733

Read Online

ACCESS | Metrics & More | Article Recommendations | SI Supporting Information

ABSTRACT: Manganese hexacyanoferrate (MnHCF) has received increasing attention as a positive electrode for either lithium- or sodium-ion storage owing to its high specific capacity among the Prussian blue analogues (PBAs). During ion release, the material undergoes the Jahn−Teller distortion arising from the oxidation of manganese to its trivalent state. Typically, the Jahn−Teller distortion is reported to destabilize the host structure of electrode materials based on layered and spinel manganese oxides, resulting in volume changes in the order of 10−20%, which deteriorate the cycle performance. Herein, the effect of such a distortion on MnHCF via operando, synchrotron powder diffraction is reported. Surprisingly, only a minor volume change (about 2%) is recorded upon cycling the electrode material against lithium, highlighting the major role of the PBA framework in stabilizing the PBAs' structures.

○ Fe
○ Mn

KEYWORDS: *operando, XRD, Prussian blue, Jahn−Teller distortion, manganese, synchrotron radiation, batteries, Li ion*
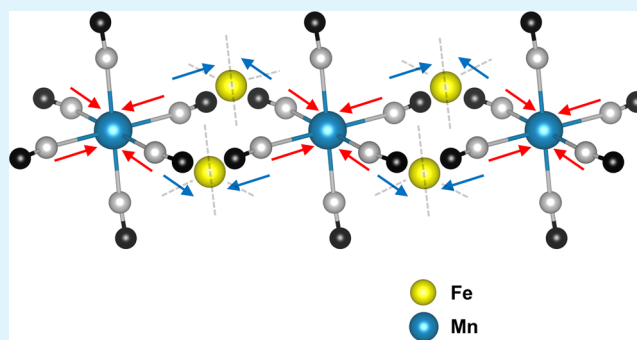
INTRODUCTION

Manganese is extensively employed as a key precursor for the development of electrochemical power sources owing to its abundance and environmental friendliness.[1] Generally, Mn-based electrode materials currently used in lithium-ion batteries (LIBs) are oxides characterized by the spinel, e.g., $LiMn_2O_4$, and layered, e.g., $Li(Ni_xCo_yMn_z)O_2$, structures, as well as their derivatives. To date, it is widely accepted that the capacity fading displayed by such compounds finds its origin in the Jahn−Teller (JT) distortion, affecting the Mn^{III} species, and in the following Mn^{2+} dissolution resulting from the disproportion of Mn^{III}.[2] Yabuuchi et al. reported a volume change of 18% upon cycling for the $P2-Na_xFe_{0.5}Mn_{0.5}O_2$ cathode material,[3] while it has been disclosed that $LiMn_2O_4$ suffers from a severe and irreversible phase transition that favors particle cracks and Mn dissolution.[4] Recently, Simonelli et al.[5] suggested an opposed trend to the expected charge compensation for the Mn centers during oxidation of lithium-rich, cobalt-poor nickel manganese oxide cathode. Here, the strain induced by the Ni oxidation on the Mn−O sublattice plays a pivotal role in triggering the Mn reduction. In this regard, various attempts have been made to alleviate the JT distortion by doping with different metal ions. A value of 10% in volume expansion is reported by Li et al. for the olivine $LiMnPO_4$,[6] while $Na_{1-x}Ni_{0.5}Mn_{0.5}O_2$ displayed an expansion of 11%.[7] The smallest volume change (7%) among the Mn-based materials has been reported for $Na_4Mn_3(PO_4)_2(P_2O_7)$.[8] Even

though this strategy contributed to suppress the volume change to some extent and to enhance the capacity retention, still these materials suffer from capacity fading upon cycling.

Considering their ability to host a large variety of ions and being easily and inexpensively synthesized, Prussian blue analogues (PBAs) have been widely employed as positive materials in electrochemical cells.[9−11] PBAs are polymeric inorganic compounds characterized by a three-dimensional open framework of repeating M′−C−N−M″−N−C− units, where both M′ and M″ are transition metals located in octahedral sites and linked together through cyanide bridges. In the case of manganese hexacyanoferrate (MnHCF), M′ is represented by Fe, while M″ is Mn. Recently,[12,13] we carried out X-ray absorption fine structure (XAFS) studies on MnHCF. According to these works, the high capacity displayed by MnHCF is the result of the electroactivity of both metallic centers. Indeed, the release of sodium ions during charge is accompanied by the change in the oxidation state of both metals, Mn and Fe, that are oxidized to their
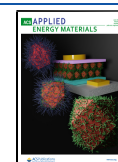
trivalent state ($Mn^{II} \rightarrow Mn^{III}$, $Fe^{II} \rightarrow Fe^{III}$) and the modification of the short-range local environment. In particular, the Mn pristine environment consists of MnN_6 octahedra with symmetric and equidistant Mn−N shells, while the extraction of Na ions introduces asymmetry and triggers a 10% Mn−N equatorial distance contraction, attributed to the JT-active Mn^{III} species, whereas the axial Mn−N distances remain roughly constant. Therefore, the JT effect is quantified as basal shrinkage rather than axial elongation. The Fe local environment (FeC_6) is, instead, less perturbated by the electrochemical process; however, the less substantial yet clear structural and electronic modifications are in line with the removal of Na ions and influenced only in the very first part of the charge by the presence of adsorbed water.[13] Despite the substantial distortion at the Mn site revealed by the XAFS local probe, both structural and electrochemical reversibilities were evidenced throughout the ion release and insertion processes. Indeed, the subsequent uptake of Na or Li ions determines the reversible reduction of the metals to their divalent state ($Mn^{III} \rightarrow Mn^{II}$, $Fe^{III} \rightarrow Fe^{II}$) and the complete return of the local structural features, regardless of the shuttling ion and/or the initial presence of the adsorbed water.

To evaluate the structural changes in the long-range order, in this manuscript we extract further insights from the synchrotron-based operando powder diffraction (XRPD) experiments on manganese hexacyanoferrate (MnHCF). Here, a lattice compensation effect is evidenced to mitigate the JT distortion upon ion release and insertion. This results in the volume change being as small as 2%, which is an unprecedented low value. The high local distortion concerning the Mn species, as revealed by XAFS, is dispersed and minimized along the PBA architecture.

■ METHODS

Synthesis. Sodium-rich manganese hexacyanoferrate (MnHCF) was synthesized through a simple and scalable co-precipitation method involving the reaction of manganese sulfate monohydrate ($MnSO_4 \cdot H_2O$) and sodium ferrocyanide decahydrate ($Na_4[Fe(CN)_6] \cdot 10H_2O$). These materials were used as received (Sigma-Aldrich) without further purification. In brief, the solutions of the two reagents (0.1 L, 0.1000 M each) were simultaneously dropwise poured in an aqueous solution (0.1 M, 0.1000 M) of sodium sulfate, Na_2SO_4 (Sigma-Aldrich), at a rate of 3.8 mL min^{-1} using a peristaltic pump. Both reagents and reaction batch were kept at constant temperature (40 ± 2 °C) using a thermostated bath. Magnetic stirring was adopted throughout the addition, which was stopped 2 min after the complete addition of the reagents. The obtained suspension containing manganese hexacyanoferrate had a pale brown color. The solution was aged for 5 days, assuring complete decantation. Then, the precipitate was collected via centrifugation at 3500 rpm for 30 min using test tubes containing about 5 mL of suspension. After removing the supernatant, the precipitate was washed three times with ~2 mL of deionized water per test tube, then ground in an agate mortar, and dried at 60 °C for 48 h.

Characterization. Thermogravimetric analysis (TGA) was carried out (TA Discovery TGA instrument) starting at 40 °C after an equilibration time of 30 min and heating to 500 °C with a ramp of 5 °C min^{-1} in a N_2 atmosphere.

Inductively coupled plasma-optical emission spectrometry (ICP-OES) was carried out by means of a Spectro Arcos FHS12 instrument. About 10 mg of the samples were dissolved in the nitric acid/hydrochloric acid solution (3/1 volumetric ratio) by heating to 200 °C in a MARS 6 iWave microwave oven. Afterward, the dissolved samples were diluted with water to achieve clear solutions, which were thermally equilibrated at 20 °C. At least two individual solutions were prepared to check the reproducibility of the results.

Electrode Preparation. The electrode slurry was prepared by mixing the active material (MnHCF, 85 wt %), conductive agent (Super C65, IMERYS, 10 wt %), and binder (poly(vinylidene difluoride), PVDF; Solef 6020, Solvay Polymerspecialties, 5 wt %). This latter component was previously dissolved in dried N-methyl-2-pyrrolidone (NMP) to form a 10 wt % solution. Additional NMP was added to adjust the viscosity of the slurry. The final solid content $\frac{m(\text{solid})}{m(\text{solid} + \text{solvent})}$ was 0.20. The materials were mixed in zirconia jars using a $\frac{m(\text{balls})}{m(\text{total solid})}$ ratio equal to 20 and following a ball milling procedure consisting of two repetitions of 1 h each with a 10 min break in between stages by means of a Pulverisette 4 Vario-Planetary mill. The slurries were cast on an aluminum foil (thickness 20 μm, previously cleaned with ethanol and dried at 80 °C overnight) using a blade coater (blade height of 200 μm) and successively dried at 60 °C overnight. Disk electrodes with a diameter of 12 mm were cut using a Hohsen puncher. The electrodes containing the MnHCF material were weighed and pressed at 10 tons for 10 s. The areal loading of the electrodes has a Student t distribution of 2.47 ± 0.04 mg_{MnHCF} cm^{-2}, considering a population of 24 electrodes, and a confidence interval equal to 0.95. Final electrodes were air-dried at 100 °C and briefly exposed to air to avoid a phase transition from the monoclinic to the rhombohedral structure.[14]

Operando Coin Cells Preparation. Commercially available stainless steel (CR2032) coin cell cases and lids were employed. Both the case and the lid of each cell were drilled, using a drill bit of diameter ϕ = 4 mm, and adequately polished by means of an abrasive drill tip. As a consequence of the abrasion, the hole was typically widened to about 5 mm. Then, two 0.25 μm thick Mylar films were glued on both the case and the lid using the poly(dimethylsiloxane) (PDMS) glue. For this purpose, a mixture 10:1 of PDMS and curing agent was prepared and thoroughly mixed for 10 min immediately before use. Curing at 60 °C overnight was performed to enable the polymer hardening.

Cell assembly occurred inside an Ar-filled glovebox (MBRAUN MB 200B ECO) with oxygen and water contents lower than 0.1 ppm. The MnHCF electrodes were assembled into the modified CR2032 coin cells, using Li metal as the negative electrode. GF/A Whatman glass felt was used as the separator to avoid the direct electrical contact between the electrodes. LP30, i.e., 1.0 M $LiPF_6$ dissolved in the 1:1 (v/v) mixture of ethylene carbonate (EC) and dimethyl carbonate (DMC) was employed as an electrolyte. Galvanostatic cycling with potential limitation (GCPL) was performed on a battery cycler (MTI eight-channel battery analyzer). The nominal capacity of 152 mAh g^{-1} (1C = 152 mAh g^{-1}) was considered for the MnHCF electrodes (i.e., containing interstitial water). Cycling was performed in the 2.3 < E < 4.3 V vs. Li^+/Li starting at an open circuit potential (OCP) with a positive initial polarization. Two full cycles were recorded in operando mode.

Operando Synchrotron X-Ray Powder Diffraction (XRPD). The previously described CR2032 coin cells were subjected to operando synchrotron X-ray powder diffraction (XRPD) in transmission mode on the MCX beamline[15] at the Elettra synchrotron light source in Trieste (Italy). The powder patterns were collected at λ = 1.33202 Å on a MAR-CCD165 area detector (80 μm pixels size), after suitable calibration using a LaB_6 standard (SRM660a from NIST), with 15 s per acquisition separated by 5 min breaks. Data reduction and analysis were carried out using GSAS-II suite.[16] Integrated patterns were analyzed by means of sequential Rietveld refinement. During this procedure, the R_{wp} values were generally found to vary in the range of 4–8%. Due to the low crystallinity and limited 2θ-range, only the fitting of the lattice parameters was allowed. A blank sample, composed by a drilled coin cell assembled without the active material, was also acquired and subtracted from the cell containing the active cathode to remove spurious features.

■ RESULTS AND DISCUSSION

As discussed in the previous work,[12] the TG analysis evidenced a double-step water loss. The first loss occurring around 100

°C is ascribable to adsorbed water, while the second, centered at 171.2 °C, is due to interstitial and structural water release.[14,17,18] From the quantitative analysis, the adsorbed and interstitial/structural water in the hydrated compound contributed to 3.7 and 8.6% to the total weight, respectively. As obtained from ICP measurements, Na/Mn/Fe ratios were equal to 1.9/1.1/1.0, leading to the $Na_{1.9}Mn_{1.1}[Fe(CN)_6]$ $2.1H_2O$ formula unit.

As reported in the literature,[14] manganese hexacyanoferrate displays two different structures depending on the hydration degree, i.e., a hydrated monoclinic phase (space group $P2_1/n$) and a completely dehydrated rhombohedral phase (space group $R\bar{3}$). Due to the substantial but not exhaustive dehydration of the electrode samples, together with the performed structural analysis, the material investigated in this work should be considered in its hydrated form.

Operando XRPD. The voltage profiles recorded upon the electrochemical ion release and insertion during the operando XRPD experiment are reported in Figure 1. By taking a closer
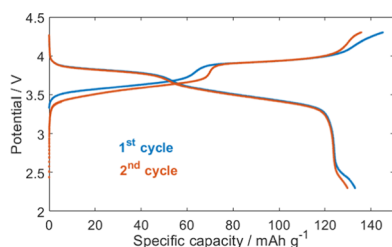

Figure 1. Charge/discharge curves of MnHCF during the XRPD operando experiment.

look at the voltage profiles during the two galvanostatic cycles, a rather complete overlap upon Li-ion insertion (cell discharge) is observed, while a slight mismatch is seen during the charge steps due to the different released ion, i.e., Na^+ in the first charge and Li^+ in the second charge.

Figure 2 summarizes the results of the XRPD experiment. The peaks at the beginning of the experiment can be easily refined to the monoclinic cell of $Na_2MnFe(CN)_6$ (s.g. $P2_1/n$, a = 10.606(3) Å, b = 7.614(7) Å, c = 7.330(6) Å, β = 91.48(4)°, V = 591.76(17) Å^3), consistent with the values obtained for the as-synthesized powder.[12]
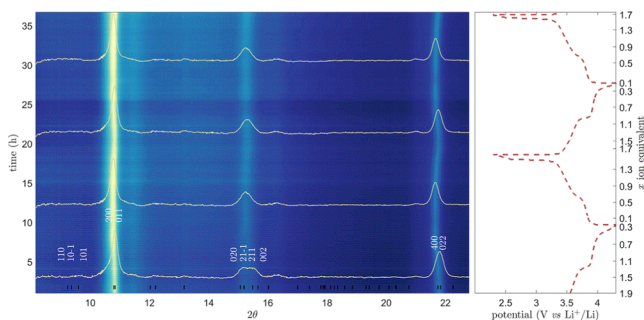

Figure 2. Operando XRPD data. Two-dimensional representation of the time-resolved operando XRPD patterns (left panel). Selected patterns are also shown, superimposed, corresponding to measures acquired after 0, 9.7, 19.4, and 29.1 h. $P2_1/n$ reflections are highlighted by black vertical tick marks, and relevant peaks are labeled in white. The concomitant cell voltage is also displayed (right panel).

No secondary phases were detected upon ion removal and insertion. The charge/discharge (C/D) profile recorded during the operando scan (see Figure 1) is consistent with a hydrated monoclinic manganese hexacyanoferrate phase as also reported by Song et al.[14] However, based on the ex situ characterization, these scientists reported the occurrence of two consecutive transitions, first to cubic and then to tetragonal phases upon Na removal (based on ex situ XRD), which is not seen here. In fact, the thorough analysis of the patterns did not evidence the presence of secondary crystalline phases. More in detail, the absence of the strongest reflection of the $R\bar{3}$ phase, expected at 12.15°, rules out its formation throughout the entire operando experiment (see also Figure 2). Small features like the weak and broad peaks at 16.3° and the shoulder near the 200 reflection at around 10.35° were already present in the blank specimen and thus identified as not belonging to the active material. All integrated patterns were Rietveld refined sequentially using the $P2_1/n$ phase. This structure can be thought to be derived from a slight distortion of the parent tetragonal lattice through a monoclinic transformation $c \approx b \approx a \cdot 2^{-1/2}$ and $\beta \approx 90°$. The monoclinic-to-cubic phase transition was not considered in our analysis based on the fact that the monoclinic angle, β, maintained a value greater than about 90.6 for the entire operando experiment, unequivocally ruling out a continuous transition toward higher symmetry. Refinement attempts carried out by adopting either a cubic or tetragonal ($a = \sqrt{2}b = \sqrt{2}c$) cell proved unsuccessful, with R_{wp} not better than 16%. Peak broadening was observed from the comparison between our data and the LaB_6 standard. The Scherrer equation for an isotropic domain model was exploited by refining, globally, all the available peaks leading to a calculated average grain size of about 35 nm. Figure 3 shows the operando evolution of the most intense couple of peaks, relatively the 200, 011 and 400, 022 reflections.

Figure 4 displays an example of the XRPD refinement carried out on the electrode during the operando experiment and the lattice parameters evolution along the ion exchange. Following the desodation process in the first charge, the 020, $21\bar{1}$, 211, and 002 reflections at around 15.3° exhibit significant changes in their relative positions, which can be attributed to a contraction of the β-angle. The lattice undergoes a smooth (but irreversible) transition, where β progressively decreases from 91.48 to about 90.9° during the first charge. This transition is completed at the end of the first charge, and for the subsequent discharge/charge cycles, β only slightly departs from the new achieved value, remaining almost constant. The trend in β-angle reflects a structural rearrangement occurring during the initial stage of Na extraction. Additionally, the c-axis increases irreversibly from the initial value of 7.33 to about 7.4 Å at ~90% of the galvanostatic charge (middle of the second plateau in the first charge). The irreversible character of these transformations suggests that the presence of interstitial water in the pristine material could be the cause of the weak structural reorganization in the course of the first charge.

During the charge process (i.e., ion removal), the cell parameter a expands about 0.6%, while a contraction of the same extent takes place during the discharge (i.e., ion insertion). In general, we observed a matching correlation between lattice changes and electrochemical evolution, in particular being the structural evolution reversible after the first structural reorganization occurring over the first charge.
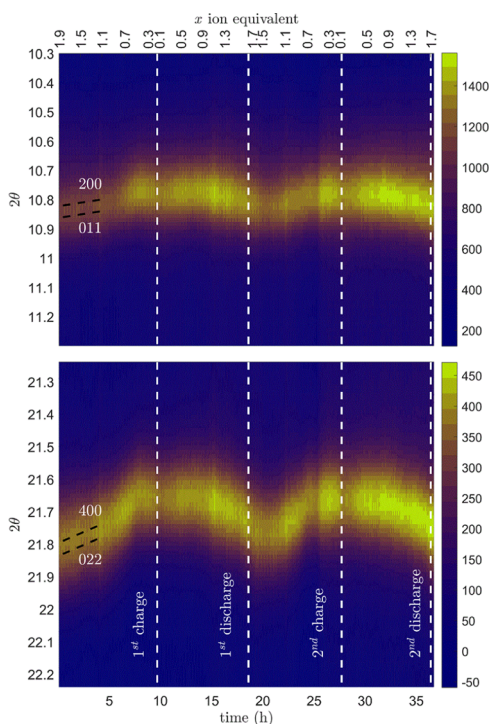
Figure 3. Magnified regions highlighting the main reflections (indexed by black dotted lines and tagged in white) responsible for the lattice expansion/contraction during the operando experiment. Contrast was increased for a better representation. Vertical dashed lines point out times at which the current was switched.

disorder, and nonoptimal instrumental conditions). On the other hand, this result is already supported by the previous XAFS study. From this operando investigation, however, is yet possible to qualitatively discuss the small changes occurring for the peaks in the 2θ range of 14.5−16° (see Figure S1), relative to the Miller's planes comprising Mn ions: (020), (21$\bar{1}$), (211), and (022). During the first charge, these peaks vary substantially both on their positions (due to lattice expansion) and relative intensities. Notably, the (21$\bar{1}$) and (211) planes additionally accommodate the cyanide species (see Figure S2).

Remarkably, the equatorial Mn−N$_{eq}$ bond lengths experienced a contraction of 10% in concomitance with the Mn^{III} species formation,[12,13] while the volume change experienced during the experiment occurs to be only 2%. This apparent disagreement underlines the capability of the Prussian blue-like lattice to compensate the pronounced variation of the Mn structural site associated with the JT-active Mn^{III} by mitigating the local structural rearrangement along the three-dimensional lattice. The non-cooperative JT (NCJT) distortion locally affects the Mn site but does not produce a macroscopic distortion in the long range, as displayed by LiNiO$_2$,[19] LiNi$_{0.85}$Co$_{0.15}$O$_2$,[20] and spinel LiMn$_2$O$_4$ above 280 K.[21] Owing to orbital ordering related to JT distortion, Radin et al.[22] have recently suggested that the NCJT distortion in LiNiO$_2$ could be due to the near-energy degeneracy of the zigzag orderings and the collinear ordering and that the nanoscale JT domains are responsible for the apparent absence of a collective distortion, contrary to NaNiO$_2$, LiMnO$_2$, and NaMnO$_2$, which feature a substantial collinear ground-state JT ordering. The overall structural stability of MnHCF is in line with other PBAs, and the NCJT distortion experimentally proven is a key advantage in employing it as electrochemical host in energy storage.

A slight increase in background was also observed proceeding along with cycling and was tentatively attributed to partial amorphisation. Overall, the peak intensities remained constant for the entire experiment, suggesting no appreciable changes in atomic occupancies (at least for the heavy elements Mn and Fe). This means that the oxidation of Mn at high voltages, i.e., during the second plateau, does not lead to electroactive material loss via dissolution in the electrolyte.
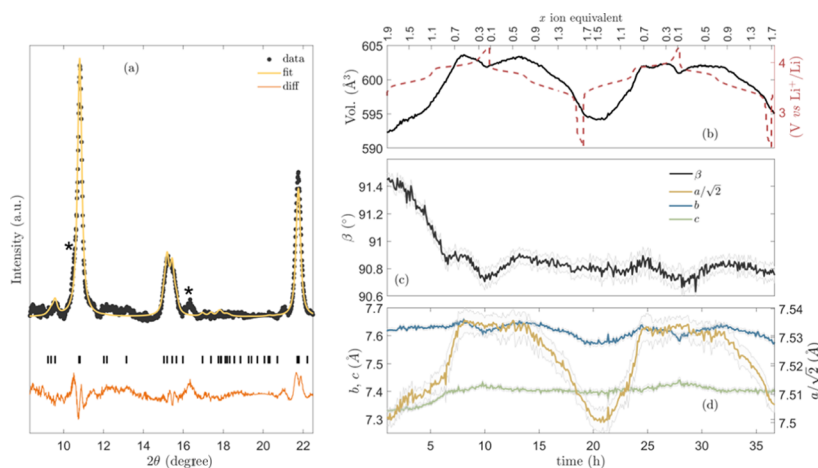
Complementing this study with the previously validated Mn and Fe electrochemical activity probed by XAFS,[12,13] the lattice distortion experienced during the ion release/uptake processes inevitably affects the surrounding of the Mn site, possibly increasing the asymmetry of the MnN$_6$ octahedral unit, thus leading to a substantial change of the Mn−N bond lengths. The structural adjustments involving the atoms around the Mn center are not relevant enough to strongly impact the XRPD patterns, especially at the low crystallographic quality achieved with these data (mostly due to low crystallinity,

Figure 4. (a) Selected Rietveld refinement on the electrode sample during operando acquisition, with black tick marks highlighting the $P2_1/n$-allowed reflections of the MnHCF structure. Asterisks highlight extrinsic features. The evolution of the cell volume (left y-axis) compared to the cell potential (right y-axis), the monoclinic angle, and the lattice parameters are reported as a function of time respectively in (b), (c), and (d), with errors reported as shades.

Indeed, unlike other Mn-active compounds, the generation of NCJT-active Mn^{3+} does not lead to any irreversible specific capacity loss. The cyanide first-shell environment around the Mn site appears to hinder the capacity fading, stabilizing the reversible oxidation to Mn^{3+} and reduction back to Mn^{2+}.

CONCLUSIONS

Contrary to the previous literature, the ion removal and uptake of manganese hexacyanoferrate appear not to involve the phase transition from monoclinic to cubic and, finally, tetragonal phase. The single-phase system is, in fact, evidenced through Rietveld refinement, showing that only the native monoclinic structure exists throughout the full charge/discharge cycle. The slight irreversible reorganization occurring at the beginning of the first alkali-ion extraction is likely due to interstitial water removal. After this, the lattice parameters evolution is fully reversible. The lattice volume expands about 2% (operando XRPD data) upon electrochemical alkali-ion removal and insertion, which appears to be in contrast with Mn−N distances previously observed to vary within 10%.[12,13] This apparent disagreement underlines, in fact, the capability of the Prussian blue-like open framework to mitigate and disperse the pronounced variation of the JT-active Mn^{III}, granting overall stability to the structure. The typical architecture of PBAs and the NCJT distortion of the Mn^{III} site compensate for the local structural distortions occurring in specific sites and promotes an overall low volume expansion/contraction.

ASSOCIATED CONTENT

Supporting Information

The Supporting Information is available free of charge at https://pubs.acs.org/doi/10.1021/acsaem.0c00669.

> Comparison between the XRPD patterns for electrodes, relevant crystallographic planes, relation between the recording time, the alkali-ion content, and the specific capacity (PDF)

AUTHOR INFORMATION

Corresponding Authors

Stefano Passerini − *Helmholtz Institute Ulm (HIU), 89081 Ulm, Germany; Karlsruhe Institute of Technology (KIT), 76021 Karlsruhe, Germany;* orcid.org/0000-0002-6606-5304; Email: stefano.passerini@kit.edu

Marco Giorgetti − *Department of Industrial Chemistry "Toso Montanari", University of Bologna, 40136 Bologna, Italy;* orcid.org/0000-0001-7967-8364; Email: marco.giorgetti@unibo.it

Authors

Angelo Mullaliu − *Helmholtz Institute Ulm (HIU), 89081 Ulm, Germany; Karlsruhe Institute of Technology (KIT), 76021 Karlsruhe, Germany;* orcid.org/0000-0003-2800-2836

Mattia Gaboardi − *Elettra - Sincrotrone Trieste S.C.p.A., 34149 Trieste, Basovizza, Italy;* orcid.org/0000-0003-3340-4469

Jasper Rikkert Plaisier − *Elettra - Sincrotrone Trieste S.C.p.A., 34149 Trieste, Basovizza, Italy*

Complete contact information is available at:
https://pubs.acs.org/10.1021/acsaem.0c00669

Author Contributions

A.M. and M. Gaboardi contributed equally to the work.

Notes

The authors declare no competing financial interest.

REFERENCES

(1) Lee, J.; Kitchaev, D. A.; Kwon, D. H.; Lee, C. W.; Papp, J. K.; Liu, Y. S.; Lun, Z.; Clément, Y. S.; Shi, T.; McCloskey, Y. S.; Guo, J.; Balasubramanian, M.; Ceder, G. Reversible Mn^{2+}/Mn^{4+} double redox in lithium-excess cathode materials. *Nature* **2018**, *556*, 185−190.

(2) Thackeray, M. M. Manganese oxides for lithium batteries. *Prog. Solid State Chem.* **1997**, *25*, 1−71.

(3) Yabuuchi, N.; Kajiyama, M.; Iwatate, J.; Nishikawa, H.; Hitomi, S.; Okuyama, R.; Usui, R.; Yamada, Y.; Komaba, S. P2-type $Na_x[Fe_{1/2}Mn_{1/2}]O_2$ made from earth-abundant elements for rechargeable Na batteries. *Nat. Mater.* **2012**, *11*, 512−517.

(4) Liu, T.; Dai, A.; Lu, J.; Yuan, Y.; Xiao, Y.; Yu, L.; Li, M.; Gim, J.; Ma, L.; Liu, J.; Zhan, C.; Li, L.; Zheng, J.; Ren, Y.; Wu, T.; Shahbazian-Yassar, R.; Wen, J.; Pan, F.; Amine, K. Correlation between manganese dissolution and dynamic phase stability in spinel-based lithium-ion battery. *Nat. Commun.* **2019**, *10*, No. 4721.

(5) Simonelli, L.; Sorrentino, A.; Marini, C.; Ramanan, N.; Heinis, D.; Olszewski, W.; Mullaliu, A.; Birrozzi, A.; Laszczynski, N.; Giorgetti, M.; Passerini, S.; Tonti, D. Role of Manganese in Lithium- and Manganese-Rich Layered Oxides Cathodes. *J. Phys. Chem. Lett.* **2019**, *10*, 3359−3368.

(6) Li, G.; Azuma, H.; Tohda, M. $LiMnPO_4$ as the cathode for lithium batteries. *Electrochem. Solid-State Lett.* **2002**, *5*, A135−A137.

(7) Komaba, S.; Yabuuchi, N.; Nakayama, T.; Ogata, A.; Ishikawa, T.; Nakai, I. Study on the reversible electrode reaction of $Na_{1-x}Ni_{0.5}Mn_{0.5}O_2$ for a rechargeable sodium-ion battery. *Inorg. Chem.* **2012**, *51*, 6211−6220.

(8) Kim, H.; Yoon, G.; Park, I.; Park, K. Y.; Lee, B.; Kim, J.; Park, Y. U.; Jung, S. K.; Lim, H. D.; Ahn, D.; Lee, S.; Kang, K. Anomalous Jahn-Teller behavior in a manganese-based mixed-phosphate cathode for sodium ion batteries. *Energy Environ. Sci.* **2015**, *8*, 3325−3335.

(9) Jiang, L.; Lu, Y.; Zhao, C.; Liu, L.; Zhang, J.; Zhang, Q.; Shen, X.; Zhao, J.; Yu, X.; Li, X.; Huang, X.; Chen, Y.; Hu, Y. S. Building aqueous K-ion batteries for energy storage. *Nat. Energy* **2019**, *4*, 495−503.

(10) Zhou, A.; Xu, Z.; Gao, H.; Xue, L.; Li, J.; Goodenough, J. B. Size-, Water-, and Defect-Regulated Potassium Manganese Hexacyanoferrate with Superior Cycling Stability and Rate Capability for Low-Cost Sodium-Ion Batteries. *Small* **2019**, *15*, No. 1902420.

(11) Nakamoto, K.; Sakamoto, R.; Sawada, Y.; Ito, M.; Okada, S. Over 2 V Aqueous Sodium-Ion Battery with Prussian Blue-Type Electrodes. *Small Methods* **2019**, *3*, No. 1800220.

(12) Mullaliu, A.; Asenbauer, J.; Aquilanti, G.; Passerini, S.; Giorgetti, M. Highlighting the Reversible Manganese Electroactivity in Na-Rich Manganese Hexacyanoferrate Material for Li- and Na-Ion Storage. *Small Methods* **2020**, *4*, No. 1900529.

(13) Mullaliu, A.; Aquilanti, G.; Conti, P.; Giorgetti, M.; Passerini, S. Effect of Water and Alkali-Ion Content on the Structure of

Manganese(II) Hexacyanoferrate(II) by a Joint Operando X-ray Absorption Spectroscopy and Chemometric Approach. *ChemSusChem* **2020**, *13*, 608−615.

(14) Song, J.; Wang, L.; Lu, Y.; Liu, J.; Guo, B.; Xiao, P.; Lee, J. J.; Yang, X. Q.; Henkelman, G.; Goodenough, J. B. Removal of interstitial H_2O in hexacyanometallates for a superior cathode of a sodium-ion battery. *J. Am. Chem. Soc.* **2015**, *137*, 2658−2664.

(15) Rebuffi, L.; Plaisier, J. R.; Abdellatief, M.; Lausi, A.; Scardi, A. P. Mcx: A synchrotron radiation beamline for X-ray diffraction line profile analysis. *Z. Anorg. Allg. Chem.* **2014**, *640*, 3100−3106.

(16) Toby, B. H.; Von Dreele, R. B. GSAS-II: The genesis of a modern open-source all purpose crystallography software package. *J. Appl. Crystallogr.* **2013**, *46*, 544−549.

(17) Ganguli, S.; Bhattacharya, M. Studies of different hydrated forms of Prussian Blue. *J. Chem. Soc., Faraday Trans. 1* **1983**, *79*, 1513−1522.

(18) Kareis, C. M.; Lapidus, S. H.; Her, J. H.; Stephens, P. W.; Miller, J. S. Non-Prussian blue structures and magnetic ordering of $Na_2Mn^{II}[Mn^{II}(CN)_6]$ and $Na_2Mn^{II}[Mn^{II}(CN)_6]\cdot 2H_2O$. *J. Am. Chem. Soc.* **2012**, *134*, 2246−2254.

(19) Rougier, A.; Delmas, C.; Chadwick, A. V. Non-cooperative Jahn-Teller effect in $LiNiO_2$: An EXAFS study. *Solid State Commun.* **1995**, *94*, 123−127.

(20) Balasubramanian, M.; Sun, X.; Yang, X. Q.; McBreen, J. In Situ X-Ray Absorption Studies of a High-Rate $LiNi_{0.85}Co_{0.15}O_2$ Cathode Material. *J. Electrochem. Soc.* **2000**, *147*, 2903.

(21) Yamada, A.; Tanaka, M.; Tanaka, K.; Sekai, K. Jahn−Teller instability in spinel Li−Mn−O. *J. Power Sources* **1999**, *81−82*, 73−78.

(22) Radin, M. D.; Van Der Ven, A. Simulating Charge, Spin, and Orbital Ordering: Application to Jahn-Teller Distortions in Layered Transition-Metal Oxides. *Chem. Mater.* **2018**, *30*, 607−618.